Electrowetting films on parallel line electrodes

Leslie Y. Yeo[1] and Hsueh-Chia Chang[2,*]
[1]*Micro/Nanophysics Research Laboratory, Department of Mechanical Engineering, Monash University, Clayton, Victoria 3800, Australia*
[2]*Department of Chemical and Biomolecular Engineering, University of Notre Dame, Notre Dame, Indiana 46556, USA*
(Received 4 April 2005; revised manuscript received 28 November 2005; published 20 January 2006)

A lubrication analysis is presented for the spreading dynamics of a high permittivity polar dielectric liquid drop due to an electric field sustained by parallel line electrode pairs separated by a distance R_e. The normal Maxwell stress, concentrated at the tip region near the apparent three-phase contact line, produces a negative capillary pressure that is responsible for pulling out a thin finger of liquid film ahead of the macroscopic drop, analogous to that obtained in self-similar gravity spreading. This front-running electrowetting film maintains a constant contact angle and volume as its front position advances in time t by the universal law $0.43R_e(t/\mathcal{T}_{cap})^{1/3}$, independent of the drop dimension, surface tension, and wettability. $\mathcal{T}_{cap}=\pi^2\mu_l R_e/8\epsilon_0\epsilon_l V^2$ is the electrocapillary time scale where μ_l is the liquid viscosity, $\epsilon_0\epsilon_l$ the liquid permittivity, and V the applied voltage. This spreading dynamics for the electrowetting film is much faster than the rest of the drop; after a short transient, the latter spreads over the electrowetting film by draining into it. By employing matched asymptotics, we are able to elucidate this unique mechanism, justified by the reasonable agreement with numerical and experimental results. Unlike the usual electrowetting-on-dielectric configuration where the field singularity at the contact line produces a static change in the contact angle consistent with the Lippmann equation, we show that the parallel electrode configuration produces a bulk negative Maxwell pressure within the drop. This Maxwell pressure increases in magnitude toward the contact line due to field confinement and is responsible for a bulk pressure gradient that gives rise to a front-running spontaneous electrowetting film.

DOI: 10.1103/PhysRevE.73.011605 PACS number(s): 68.15.+e, 41.20.Cv, 47.85.Dh

I. INTRODUCTION

The ability to control the wettability of a liquid, ideally without mechanically moving parts, is paramount in the actuation of fluids in microfluidic devices. This has prompted a recent resurgence in studies on electrowetting, which allows a rapid, reversible, and precise means for manipulating small liquid volumes with relatively low power consumption [1]. The success in generating fluid velocities in excess of several cm/s has also attracted significant interest in electrowetting for other applications such as electrostatic-assist coating [2] and miniature optical focusing devices [3].

Attempts have been made to relate experimental observations of electrowetting on a wide variety of dielectric or polymer substrates by correlating the measured change in the contact angle θ [4,5] against the Lippmann equation [6]

$$\cos\theta=\cos\theta_0+\frac{\epsilon_0\epsilon_l V^2}{2d\gamma}, \tag{1}$$

where θ_0 is the contact angle in the absence of an electric field, ϵ_0 the permittivity of free space, ϵ_l the liquid dielectric permittivity, V the applied potential, d the dielectric film thickness, and γ the vapor-liquid interfacial tension. Several theoretical interpretations, based on molecular kinetic [4,7], electromechanic [8–10], and static [11] analyses, have since been proposed to describe the static change in the macroscopic contact angle under the influence of an applied electric field.

In electrowetting-on-dielectric configurations where the drop is placed above a dielectric film coated planar electrode [Fig. 1(a)], however, the weakly singular vapor phase electric field that arises is confined to a small region with a length scale comparable to d [12,13]. The Maxwell pressure gradient that results, therefore, is localized and microscopic, giving rise to a point force at the contact line. This point force exactly balances the surface forces and hence there is no net force that can result in bulk liquid motion. Consequently, only a static change in the macroscopic contact angle is possible [14]. In contrast, we show in this paper that when a parallel line electrode configuration is adopted, as shown in Fig. 1(b) [15,16], a nonsingular liquid phase electric field, which decays linearly away from the contact line as the film increases in height, can give rise to a macroscopic Maxwell pressure gradient that extends into the bulk region. As a result, the bulk forces are no longer balanced by the surface forces at the contact line and hence the negative Maxwell pressure gradient induces bulk liquid motion by spontaneously pushing out a thin front-running electrowetting film [14]. A formulation distinct from that developed for electrowetting on dielectric film coated planar electrodes that accounts for a hydrodynamic mechanism to predict the formation and propagation of these spontaneous electrowetting films is therefore required.

In this paper, we present a model that bridges the electrokinetic and wetting hydrodynamic theories to predict the spreading dynamics of these spontaneous electrowetting films for the parallel line electrode configuration. The wetting dynamics is shown to be analogous to gravity spreading; the Maxwell pressure term arising due to the applied electric field appears as an extra body force term in the normal stress balance. We observe, from our numerical simulations, that

*Corresponding author. Electronic address: hchang@nd.edu

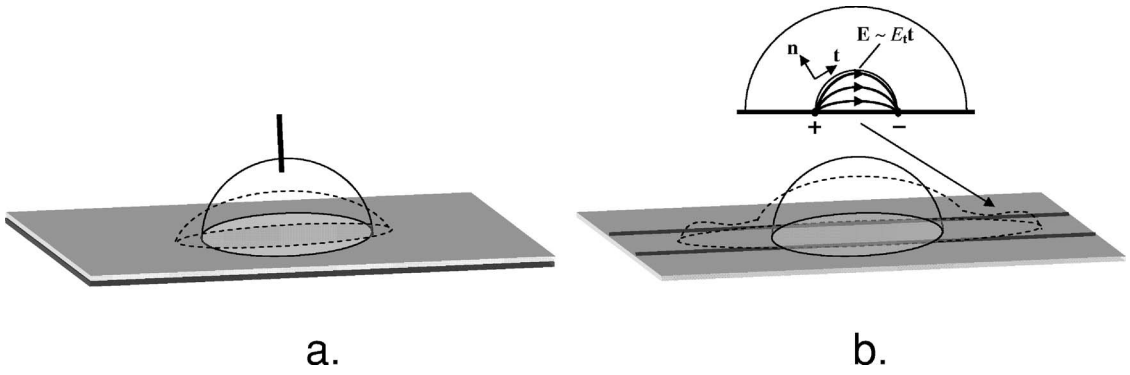

FIG. 1. Typical electrode configurations used in electrowetting experiments. (a) Static change in the macroscopic contact angle obtained using dielectric film coated planar electrodes. (b) Spontaneous electrowetting film produced using a parallel line electrode configuration. The inset shows a schematic representation of the cross section of the bulk drop and electrowetting film and the associated electric field lines which are predominantly tangential at the interface, i.e., $\mathbf{E}=E_{\mathbf{t}}\mathbf{t}$, where $\mathbf{E}$ is the electric field vector, $E_{\mathbf{t}}$ is the tangential field component, and $\mathbf{n}$ and $\mathbf{t}$ are the unit normal and tangent vectors to the interface, respectively.

this Maxwell stress rapidly pulls out a thin front-running electrowetting film, whose thickness exceeds molecular dimensions. This electrowetting film advances more rapidly than the bulk of the drop, similar to the fingers observed in gravity and viscous spreading [17,18].

The model is formulated in Sec. II. In Sec. III, the thin electrowetting film front of approximately constant volume that is pulled out by the Maxwell stress ahead of the macroscopic drop is shown to behave in a self-similar manner. We then numerically validate the self-similar behavior of the electrowetting film in Sec. IV. Matched asymptotics are subsequently employed in Sec. V to elucidate the mechanisms behind the spreading phenomenon where we obtain scaling laws for the spreading dynamics of the liquid drop that are consistent with numerical and experimental results.

II. BASIS AND FORMULATION

A. Governing equations

The spreading of a high permittivity polar dielectric Newtonian liquid drop with volume $\mathcal{V}$ and of constant density ρ_l and viscosity μ_l, lying on a horizontal rigid and impermeable solid substrate, under electrocapillary action is studied. The electrode configuration used in Jones *et al.* [15], in which the electric field is predominantly tangential to the three-phase contact line, as shown in Fig. 2, is considered. The two parallel line electrodes, separated by a distance R_e, are placed horizontally on the solid substrate in the direction of the flow and orthogonal to the contact line.

The electrowetting film pulled out ahead of the macroscopic drop, assumed to be of constant width, is considered sufficiently slender such that we can define a small parameter $\varepsilon \equiv \tilde{\mathcal{H}}/\tilde{\mathcal{L}} \ll 1$; $\tilde{\mathcal{H}}$ and $\tilde{\mathcal{L}}$ are the characteristic height and length scales of the electrowetting film over which the Maxwell stress decays away from the contact line, to be defined subsequently. The slender film then suggests that the usual lubrication approximation holds in the long-wave limit where $\varepsilon \to 0$. In addition, the cross section of the film, as depicted by the plane *ABCD* in the inset of Fig. 2, can be approximated by a thin rectangular geometry where $y \sim R_e \sim \tilde{\mathcal{L}}$. Ignoring boundary effects in the y direction, we thus adopt a planar model with predominantly x-z dependent hydrodynamics.

The Maxwell force $\mathbf{F}$ due to a dc or ac electric field, also known as the Korteweg-Helmholtz force density [19,20], can be expressed by

$$\mathbf{F} = \rho_f \mathbf{E} - \frac{\epsilon_0}{2} \nabla \left[\epsilon - \rho \left(\frac{\partial \epsilon}{\partial \rho} \right)_T \right] \mathbf{E} \cdot \mathbf{E}, \tag{2}$$

where ϵ is the dielectric permittivity, T the temperature, and ρ the density of the body. The electric field vector $\mathbf{E}=-\nabla\phi = E_{\mathbf{n}}\mathbf{n}+E_{\mathbf{t}}\mathbf{t}$, where ϕ is the electric potential, and $E_{\mathbf{n}}$ and $E_{\mathbf{t}}$ are the normal and tangential components of the electric field; $\mathbf{n}$ and $\mathbf{t}$ are the unit normal and tangent vectors, respectively. In dielectric liquids, the net free space charge density ρ_f and hence the Coulombic force term are typically negligible. The incompressibility of the fluid also renders the electrostriction term $\partial\epsilon/\partial\rho$ negligible.

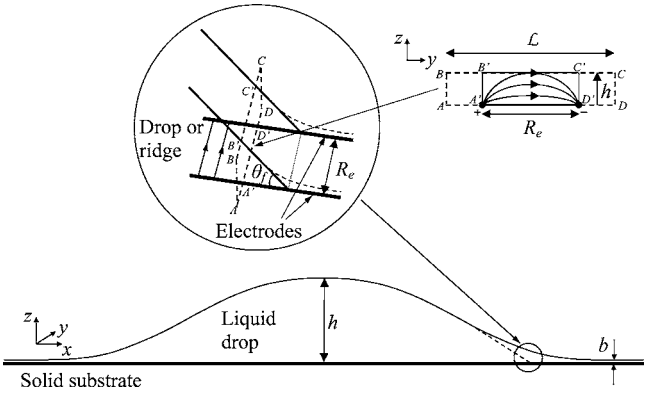

FIG. 2. Schematic representation of the spreading liquid drop over a horizontal substrate layer for the case of parallel electrode configurations. The inset depicts the wedgelike geometry of the drop or the capillary ridge of the electrowetting film in the three-phase contact line region. The plane *ABCD* is a y-z cross section of this liquid wedge schematically depicting the field lines that arise in the liquid, which are tangential to the contact line.

Given the absence of free space charge, the electrostatic potential ϕ obeys the Laplace equation

$$\nabla^2 \phi_i = 0, \tag{3}$$

where $i=g,l$ describes the ambient and liquid phases, respectively. The boundary conditions are stipulated by continuity of the normal and tangential fields across the interface Γ:

$$\left[\epsilon_0 \epsilon_i \frac{\partial \phi_i}{\partial \mathbf{n}} \right]_g^l = \left[\frac{\partial \phi_i}{\partial \mathbf{t}} \right]_g^l = 0 \quad \text{on } \Gamma, \tag{4}$$

where ϵ_i is the dielectric constant of phase i and the square brackets $[\cdot]_g^l$ indicate a jump in the inner quantity across the interface. The liquid phase hydrodynamics, on the other hand, are governed by the mass and momentum conservation equations:

$$\boldsymbol{\nabla} \cdot \mathbf{u} = 0, \tag{5}$$

$$\rho_l (\mathbf{u}_t + \mathbf{u} \cdot \boldsymbol{\nabla} \mathbf{u}) = \boldsymbol{\nabla} \cdot \mathbf{T}, \tag{6}$$

where $\mathbf{u}$ is the liquid phase velocity field and t is the time. Henceforth, the subscripts x, y, z, and t will be used to denote partial differentials with respect to these spatial and temporal variables. $\mathbf{T}$ is the total stress tensor, comprised of the deviatoric stress tensor, the viscous stress tensor $\mathbf{T}_v = \mu(\boldsymbol{\nabla}\mathbf{u} + \boldsymbol{\nabla}\mathbf{u}^T)$, μ being the viscosity, and the Maxwell stress tensor $\mathbf{T}_M$:

$$\mathbf{T} = -p\mathbf{I} + \mathbf{T}_v + \mathbf{T}_M, \tag{7}$$

where p is the pressure and $\mathbf{I}$ is the unit tensor. The Maxwell stress tensor can be obtained from Eq. (2), in which, for incompressible fluids, the ponderomotive force term arises solely due to inhomogeneity in the dielectric permeability:

$$\mathbf{T}_M = \epsilon_0 \epsilon \mathbf{E}\mathbf{E} - \frac{\epsilon_0 \epsilon}{2} (\mathbf{E} \cdot \mathbf{E}) \mathbf{I}. \tag{8}$$

To satisfy irrotationality of the electric field $\boldsymbol{\nabla} \cdot \mathbf{E} = 0$, Eq. (6) becomes

$$\rho_l (\mathbf{u}_t + \mathbf{u} \cdot \boldsymbol{\nabla} \mathbf{u}) = -\boldsymbol{\nabla} p + \mu_l \nabla^2 \mathbf{u}, \tag{9}$$

with the velocities satisfying the no-slip boundary condition on the solid substrate Γ_s at $z=0$:

$$\mathbf{u} = \mathbf{0}. \tag{10}$$

In addition, the kinematic boundary condition applies at the interface Γ, where $z=h$, h being the thickness of the liquid film:

$$h_t + (h\bar{u})_x + (h\bar{w})_y = v; \tag{11}$$

$\bar{u}$ and $\bar{w}$ are the streamwise and transverse velocities, respectively, cross-sectional averaged across the height of the film, and v is the velocity in the vertical direction. The following normal and tangential stress boundary conditions also apply on Γ:

$$[\mathbf{n} \cdot \mathbf{T} \cdot \mathbf{n}]_g^l = \kappa \tag{12}$$

and

$$[\mathbf{t} \cdot \mathbf{T} \cdot \mathbf{n}]_g^l = 0, \tag{13}$$

where

$$\kappa = \gamma_l \boldsymbol{\nabla} \cdot \mathbf{n} \tag{14}$$

is twice the mean interfacial curvature of the flat electrowetting film, γ_l being the interfacial tension at the gas-liquid interface.

B. Dimensionless equations

We utilize the following transformations to render the problem dimensionless:

$$x \to \tilde{\mathcal{L}} x, \quad y \to \tilde{\mathcal{L}} y, \quad \text{and } (z,h) \to \tilde{\mathcal{H}}(z,h). \tag{15}$$

The velocities, on the other hand, scale as

$$u \to \mathcal{U} u, \quad v \to \varepsilon \mathcal{U} v, \quad \text{and } w \to \mathcal{U} w, \tag{16}$$

respectively, where $\mathcal{U} \equiv \varepsilon^3 \gamma_l / \mu_l$ is the characteristic velocity. p is scaled as $\varepsilon \gamma_l / \tilde{\mathcal{L}}$ and t scales as $\tilde{\mathcal{L}} / \mathcal{U}$. In addition, we scale the electric potential ϕ with the applied voltage V and the electric field E by the characteristic potential drop across the electrodes V/R_e. This set of scalings was chosen in order to demote the pressure to the same order as the capillary stress such that the relative contributions of the Maxwell stress to the capillary stress can be described by a single parameter δ, to be defined below.

The dimensionless Laplace equation in Eq. (3) and the associated boundary conditions given by Eq. (4) then read

$$\varepsilon^2 \phi_{i_{xx}} + \varepsilon^2 \phi_{i_{yy}} + \phi_{i_{zz}} = 0 \tag{17}$$

and

$$\left[\epsilon_0 \epsilon_i \frac{\partial \phi_i}{\partial z} \right]_g^l = \left[\frac{\partial \phi_i}{\partial y} \right]_g^l = 0 \quad \text{on } \Gamma, \tag{18}$$

noting that $\mathbf{n}$ and $\mathbf{t}$ are defined in the transverse cross section and point in the z and y directions, respectively, in the lubrication limit. Due to the electrode configuration, the scaling in Eq. (15) is actually inappropriate for the electric potential and the Laplace equation despite being appropriate for the hydrodynamics. We shall hence rescale Eq. (17) subsequently.

For the hydrodynamic problem, we shall assume the side contact lines of the electrowetting film to be stationary and hence there is no velocity or motion in the y direction. In fact, the electrowetting film is assumed to be sufficiently flat such that the film thickness h is independent of y. As such, only the velocities (u,v) in the x and z directions need to be resolved and they obey the following mass and momentum conservation equations when Eqs. (5) and (9) are rendered dimensionless using the scalings defined above:

$$u_x + v_z = 0, \tag{19}$$

$$\varepsilon^2 \mathrm{Re}(u_t + u u_x + v u_z) = -p_x + \varepsilon^2 u_{xx} + u_{zz}, \tag{20}$$

and

$$\varepsilon^4 \mathrm{Re}(v_t + uv_x + vv_z) = -p_z + \varepsilon^4 v_{xx} + \varepsilon^2 v_{zz}, \tag{21}$$

where $\mathrm{Re} \equiv \rho_l \mathcal{U}\tilde{\mathcal{L}}/\mu_l$ is the Reynolds number, which is of order unity or smaller with respect to ε. In addition, the boundary conditions given by Eqs. (10) and (11) can be expressed as

$$u = v = 0 \quad \text{on } \Gamma_s \tag{22}$$

and

$$h_t + (h\bar{u})_x = v \quad \text{on } \Gamma. \tag{23}$$

As a consequence of Eqs. (12)–(14) together with Eq. (8), the dimensionless normal and tangential stress balances on Γ become

$$p = \frac{h_{xx}}{(1+\varepsilon^2 h_x^2)^{3/2}} - 2[\varepsilon^2(v_z - u_z h_x) + \varepsilon^4(u_x h_x - v_x)h_x] + \frac{\pi^2 \delta}{16} p_M, \tag{24}$$

and

$$\varepsilon^2(v_z - u_x)h_x + \frac{1-\varepsilon^2 h_x^2}{2}(u_z + \varepsilon^2 v_x) = 0, \tag{25}$$

respectively, where p_M is the dimensionless Maxwell pressure, to be defined subsequently. We observe that the above equations introduce two small parameters: $\zeta \equiv \epsilon_g/\epsilon_l$ as a consequence of Eqs. (12), (13), and (18) with Eq. (8) as the permittivity ratio, and,

$$\delta \equiv \frac{8\epsilon_0 \epsilon_l V^2 \tilde{\mathcal{L}}}{\varepsilon \pi^2 \gamma_l R_e^2}, \tag{26}$$

in Eq. (24) is the Maxwell Bond number, which defines the relative contributions between the Maxwell and capillary stresses. For high permittivity polar dielectrics such as deionized water which was used in the experiments of Jones *et al.* [15] and Ahmed *et al.* [16], $\zeta \ll 1$. Moreover, we note that $1/\delta$ is also small in the contact line region.

Noting that both $\zeta \sim O(\varepsilon)$ and $1/\delta \sim O(\varepsilon)$ for most experimental conditions, it is then possible to assume a regular perturbation expansion of all the variables in the asymptotically small ε limit:

$$(u, v, p, p_M, \phi_i) = (u^{(0)}, v^{(0)}, p^{(0)}, p_M^{(0)}, \phi_i^{(0)}) + \varepsilon(u^{(1)}, v^{(1)}, p^{(1)}, p_M^{(1)}, \phi_i^{(1)}) + \cdots. \tag{27}$$

Substitution into Eqs. (17)–(25) then yields the leading order governing equations and associated boundary conditions. In the slender body limit and for $1/\delta \ll 1$, the electrostatic and hydrodynamic problems can be solved separately. However, we will show that the Maxwell stress is still coupled to the film thickness and hence the hydrodynamics of the film. We now proceed to consider the leading order electrostatic and hydrodynamic formulations in turn.

C. Leading order electrostatic model

Since $\epsilon_l \gg \epsilon_g$ for high permittivity polar dielectric liquids, it can be seen from Eqs. (8), (12), and (13) that the liquid and gas phase normal fields $E_{\mathbf{n}_l}$ and $E_{\mathbf{n}_g}$ at the interface are negligible. Moreover, since $E_{\mathbf{t}_g} = E_{\mathbf{t}_l} = E_{\mathbf{t}}$ from continuity of the tangential electric stresses in Eq. (18), $\epsilon_l E_{\mathbf{t}_l} \gg \epsilon_g E_{\mathbf{t}_g}$ and hence only the liquid phase tangential electric field contributes to the Maxwell pressure. From Eqs. (8) and (12), the leading order dimensionless Maxwell pressure $p_M^{(0)}$ then becomes

$$p_M^{(0)} = -E_{\mathbf{t}}^2. \tag{28}$$

We note that a normal surface force results even in the absence of a finite normal field $E_{\mathbf{n}}$ at the interface. This is because the ponderomotive force is a body force term that arises due to induced polarization within the bulk of the liquid and produces an internal normal force. The solution for the gas phase field, which is extremely weak compared to the liquid field, is then not required to obtain the desired Maxwell pressure in Eq. (28) to leading order.

The tangential field $E_{\mathbf{t}}$ is not uniform along the interface. However, if it is nearly uniform and if the interface cross section is circular, as we shall assume subsequently, the resulting Maxwell pressure will change the radius of curvature of the circle. Under such limiting conditions, the change in the curvature of the circle can be interpreted as an electrocapillary effect, i.e. the Maxwell stress results in a change in the surface tension. Such electrocapillary effects have indeed been observed experimentally [6]. Strictly speaking, however, the Maxwell pressure given by Eq. (28) is unrelated to the curvature and hence cannot be related to a change in the surface tension.

A formal slender electrowetting film expansion in ε, as given by Eq. (27), can be carried out for the scaled version of the liquid phase Laplace equation in Eq. (17). However, due to the polarity of the electrodes, the transverse y dependence is actually stronger than that in the x direction for the electrostatic problem. A more appropriate scaling for y and R_e is such that $\tilde{\mathcal{H}} \ll (y, R_e) \ll \tilde{\mathcal{L}}$ or $(y/\tilde{\mathcal{L}}) \sim (R_e/\tilde{\mathcal{L}}) \sim \varepsilon^{1/2}$ for the slender electrowetting film. This more refined scaling was unnecessary for the hydrodynamics because the electrowetting film is flat and the transverse y dependence is hence absent. This proper scaling also gives rise to a dimensionless Laplace equation for the liquid phase of the form

$$\varepsilon^2 \phi_{l_{xx}} + \varepsilon \phi_{l_{yy}} + \phi_{l_{zz}} = 0, \tag{29}$$

such that the longitudinal x dependence can be omitted. However, instead of solving the planar Laplace equation in the y-z coordinate given in Eq. (29) by a regular expansion in ε, we shall use the same length scale and scaling for the two coordinates, derive a full two-dimensional solution, and then simplify it with an expansion for the slender electrowetting film.

Defining $\tilde{y} = y/\varepsilon$, Eqs. (17) and (18) for the liquid phase become

$$\phi_{l_{\tilde{y}\tilde{y}}} + \phi_{l_{zz}} = 0, \tag{30}$$

with

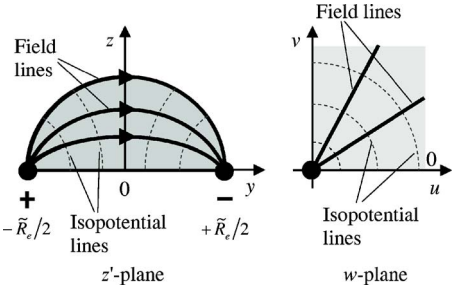

FIG. 3. (Color online) Mapping of the semicircular electrowetting film cross section with insulated boundaries at the interface and at the solid substrate in the z' plane onto the upper right quadrangle of the rectangular w plane.

$$\frac{\partial \phi_l}{\partial \mathbf{n}} = 0 \quad \text{on } \Gamma \text{ and } \Gamma_s. \tag{31}$$

In addition, we impose a further boundary condition for the constant potential line electrodes placed on the solid substrate Γ_s at $\tilde{y} = \pm \tilde{R}_e/2$, where $\tilde{R}_e \equiv \tilde{R}_e/\tilde{\mathcal{H}}$ is the dimensionless electrode separation which has been scaled by the characteristic film height:

$$\phi_l = \pm 1 \quad \text{at } \tilde{y} = \mp \tilde{R}_e/2 \text{ and } z = 0. \tag{32}$$

We proceed by solving the leading order problem given by Eq. (30) subject to the boundary conditions in Eqs. (31) and (32) in the $\tilde{y}$-z plane $ABCD$ for the geometry shown in the inset of Fig. 2. In this plane, the two line electrodes are represented by two point charges placed on the solid substrate and separated by a distance $\tilde{R}_e$. We will concern ourselves only with the region of the advancing electrowetting film near the contact line. As such, the film height is much smaller than the capillary length and hence gravity is unimportant. The cross section of the film hence obeys the static Laplace-Young equation, i.e., it is a circular arc with two ends pinned to the electrodes. Such a static circular arc description is consistent with experimental observations [15,16] and has been employed in other lubrication theories describing rivulet dynamics [21,22]. Assuming this geometry, it is then possible to solve Eq. (30) with Eqs. (31) and (32) using conformal mapping.

We shall first consider a semicircular arc geometry and show that the more slender circular arc solutions for the field lines are contained in this formulation. The semicircular cross section geometry in which the boundaries of the semicircle and base are insulated and the electrodes can be represented by point charges at the equatorial ends of the semicircle can be mapped onto the right top quadrangle of the rectangular w plane, as shown in Fig. 3. This is done by the following linear fractional transformation [23]:

$$w = f(z') = \frac{\tilde{R}_e/2 + z'}{\tilde{R}_e/2 - z'}. \tag{33}$$

The notation z' corresponds to the original plane domain and is to be distinguished from the vertical coordinate z. The boundary $|z'| = \tilde{R}_e/2$ is then mapped onto the boundary $u = 0$ which is the upper right quadrangle of the v axis. The complex potential is then given by

$$F(z') = \Phi(x,y) + i\Psi(x,y), \tag{34}$$

where Φ is the potential in which $\Phi = \text{const}$ surfaces are equipotential surfaces and Ψ is its conjugate harmonic, which describes orthogonal trajectories to the constant potential lines (i.e., field lines); both Φ and Ψ are uniquely related through the Cauchy-Reimann equations. $F(z')$ for the mapping described above is then given by Kreyszig [23], from which we obtain

$$\Psi(x,y) = \mathrm{Re}[F(z')] = \frac{2}{\pi}\left[\tan^{-1}\left(\frac{z}{\tilde{R}_e/2 + y}\right) - \tan^{-1}\left(\frac{z}{\tilde{R}_e/2 - y}\right)\right]. \tag{35}$$

The tangential liquid electric field can then be determined using the Cauchy-Reimann equations:

$$E_{\mathbf{t}} = -\frac{2z\tilde{R}_e}{\pi}\left(\frac{1}{(\tilde{R}_e/2 + \tilde{y})^2 + z^2} + \frac{1}{(\tilde{R}_e/2 - \tilde{y})^2 + z^2}\right). \tag{36}$$

We note from Fig. 3 that the solution for the semicircle geometry given by Eq. (35) describes field lines that are circular arcs and they correspond to cross sections with interfacial height $z = h$ smaller than the semicircle. Evaluating $E_{\mathbf{t}}$ at the center point between the electrodes $\tilde{y} = 0$ where the field is purely tangential and at different interfacial heights h, and expanding in the limit of laterally slender films where $h/\tilde{R}_e \to 0$ and $\varepsilon \to 0$, we obtain, noting $E_{\mathbf{t}}^2$ is required,

$$E_{\mathbf{t}}^2 = \frac{256h^2}{\pi^2 \tilde{R}_e^{\,2}}\left(1 - \frac{8h^2}{\tilde{R}_e^{\,2}}\right)^2. \tag{37}$$

The expansion in the small $h/\tilde{R}_e$ limit thus removes any tangential field dependence in the $\tilde{y}$ direction. If θ_f is the contact angle at the wedge tip at $x = x_f$, then $h = \varepsilon(x_f - x)\tan\theta_f$, and, hence from Eq. (28),

$$p_M^{(0)} = -\frac{256(x_f - x)^2 \tan^2\theta_f}{\varepsilon^2 \pi^2 \tilde{R}_e^{\,2}}\left(1 - \frac{16\tan^2\theta_f}{\varepsilon^2 \tilde{R}_e^{\,2}}(x_f - x)^2\right), \tag{38}$$

suggesting that the interfacial field decays linearly along the interface away from the tip at $x = x_f$. The Maxwell stress in Eq. (38) is responsible for pulling out a thin front-running electrowetting film ahead of the macroscopic drop. From Eq. (38), we observe the manner in which the Maxwell stress decays from the electrowetting film front to be dependent on $\tan^2\theta_f$ or h^2 and $\tilde{R}_e^2$. This arises because the interfacial tangential field at the contact line $2/\tilde{R}_e$ decreases by a factor $\tilde{R}_e^2/(\tilde{R}_e^2 + h^2)$ as the interfacial field arc lines increase in length with the increasing film thickness. It is then possible to obtain a length scale over which the Maxwell stress decays to zero; setting $p_M = 0$,

$$x_f - x \sim \frac{\varepsilon \tilde{R}_e}{4 \tan \theta_f}, \tag{39}$$

such that Eq. (38) becomes

$$p_M^{(0)} = -\frac{16}{\pi^2}\left(1 - \frac{16 \tan^2 \theta_f}{\tilde{R}_e^{\,2}}(x_f - x)^2\right). \tag{40}$$

Returning to dimensional coordinates, Eq. (39) becomes

$$x_f - x \sim \tilde{\mathcal{L}} = \frac{R_e}{4 \tan \theta_f}, \tag{41}$$

which is the characteristic length scale we have chosen over the x direction. At a distance beyond $\mathcal{L}$ from the front, we assume the Maxwell stress vanishes completely and we remove the linear expansion in Eq. (40) in our simulation and theory.

We can also estimate the magnitude of the volume per unit width of the initial mass of electrowetting film V_0 pulled out from the macroscopic drop. This initial mass should have a length equal to the decay length scale $\tilde{\mathcal{L}}$:

$$V_0 \sim \tilde{\mathcal{H}}\tilde{\mathcal{L}} \sim \tilde{\mathcal{L}}^2 \tan \theta_f \sim \frac{R_e^2}{16 \tan \theta_f}, \tag{42}$$

where

$$\tilde{\mathcal{H}} \sim \tilde{\mathcal{L}} \tan \theta_f. \tag{43}$$

It will be shown that as the electrowetting film advances, its volume remains relatively constant at V_0 although a small fraction of liquid does enter the electrowetting film due to partial drainage from the bulk macroscopic drop. As the electrowetting film spreads, the angle θ_f will be shown to remain constant at the initial value when the initial volume of liquid is pulled out of the drop.

D. Leading order hydrodynamic model

From the expansions given in Eq. (27), Eqs. (19)–(22) and Eq. (25) lead to the following dimensionless leading order equations:

$$u_x^{(0)} + v_z^{(0)} = 0, \tag{44}$$

$$p_x^{(0)} = u_{zz}^{(0)}, \tag{45}$$

and

$$p_z^{(0)} = 0, \tag{46}$$

together with the no slip boundary condition on Γ_s:

$$u^{(0)} = v^{(0)} = 0 \quad \text{at } z = 0, \tag{47}$$

and the shear-free boundary condition on Γ:

$$u_z^{(0)} = 0 \quad \text{at } z = h. \tag{48}$$

From Eq. (46), $p^{(0)} = p^{(0)}(x)$, consistent with the leading order Maxwell pressure derived in Eq. (40) for a laterally slender film where $h/\tilde{R}_e \ll 1$. Utilizing Eqs. (40) and (48) in Eq. (24), the leading order normal stress jump on Γ becomes

$$p^{(0)} = h_{xx} - \delta[1 - \chi(x_f - x)^2]. \tag{49}$$

Here,

$$\chi \equiv \frac{16 \tan^2 \theta_f \tilde{\mathcal{L}}^2}{R_e^2} \tag{50}$$

is the linear Maxwell stress decay factor controlling the distance from the tip x_f over which the tangential electric field at the interface linearly decays. Finally, the kinematic boundary condition in Eq. (23) reads

$$h_t + (h\overline{u^{(0)}})_x = 0 \quad \text{at } z = h. \tag{51}$$

We integrate Eq. (45) twice with the boundary conditions given by Eqs. (47) and (48) to yield a parabolic velocity profile for the streamwise velocity:

$$u^{(0)} = \left(\frac{z^2}{2} - zh\right)p_x^{(0)}. \tag{52}$$

Equations (51) and (52) then result in the evolution equation for the interfacial height of the drop:

$$h_t = (h^3 p_x^{(0)})_x/3. \tag{53}$$

Details of the numerical solution of Eq. (53) with Eq. (49) will be presented in Sec. IV. We first report the important numerical finding that the apparent contact angle at the advancing electrowetting film front θ_f and the linear Maxwell stress decay factor χ are roughly constant with respect to time by initially allowing χ to vary with θ_f in the preliminary simulations. Figure 4(a) shows that θ_f does not vary signficantly in time and has an average value of approximately 0.524, suggesting that variations in χ as the film front propagates are insignificant; we will therefore set χ to be constant in our simulations henceforth.

There are physical reasons why θ_f is time invariant for the advancing electrowetting film. It will be apparent in the numerical results that a sharp capillary ridge forms at the leading edge of the front-running electrowetting film, for which a static limit exists where the Maxwell and capillary pressures balance to yield a locally constant static contact angle θ_f. This is the same angle as the linear wedge angle defined above when the initial volume is pulled out. The dominant balance between Maxwell pressure in Eq. (40) and capillarity in this wedge region where $x \sim x_f$ then reads

$$\frac{\gamma_l \mathcal{H}_{cap}}{\mathcal{L}_{cap}^2} \sim \frac{8\epsilon_0 \epsilon_l V^2}{\pi^2 R_e^2}, \tag{54}$$

where

$$\mathcal{H}_{cap} \sim \tan \theta_f \mathcal{L}_{cap} \tag{55}$$

is the height of the capillary ridge, and

$$\mathcal{L}_{cap} \equiv \frac{\pi^2 \gamma_l R_e^2}{8\epsilon_0 \epsilon_l V^2} \tag{56}$$

is the electrocapillary length scale for the width of the ridge, obtained by noting that the ridge curvature is $1/\mathcal{L}_{cap}$ and the

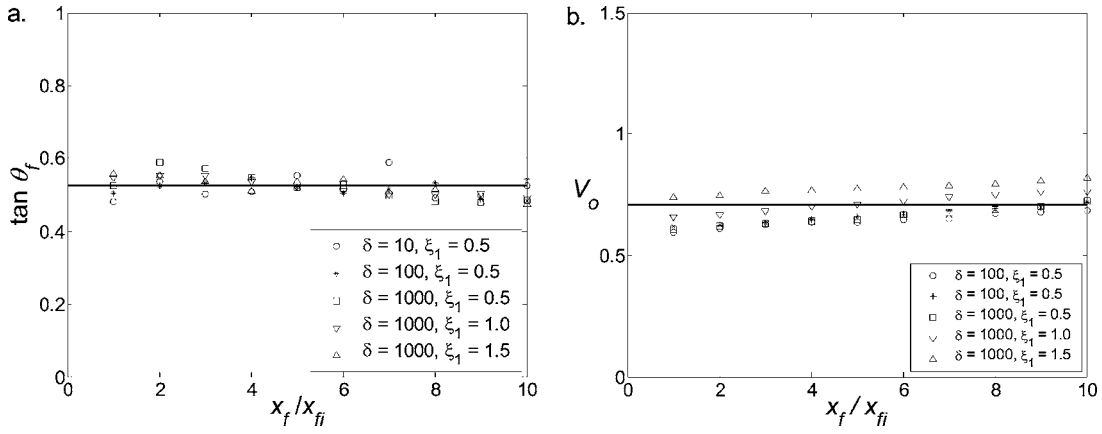

FIG. 4. Variation of (a) the contact angle at the electrowetting film front tan θ_f, and (b) the dimensionless volume of the electrowetting film V_0, as a function of the advancing film front x_f/x_{fi} which propagates forward with time; x_{fi} is the initial front position.

capillary pressure $\gamma_l/\mathcal{L}_{cap}$ must balance the Maxwell pressure $8\epsilon_0\epsilon_l V^2/\pi^2 R_e^2$. The curvature at the slope on the left side of Eq. (54) is, in essence, matched to a cylinder of radius $\mathcal{L}_{cap}$ at the ridge, as in the Bretherton problem [24]. It then follows from Eqs. (26), (55), and (56) that

$$\delta = \frac{\tilde{\mathcal{L}}}{\mathcal{L}_{cap}}, \tag{57}$$

and $\tan\theta_f \sim O(1)$, consistent with the numerical value of 0.524. Equation (57) therefore relates the Maxwell stress decay length scale to the electrocapillary length scale; a schematic diagram showing the electrowetting film region as it initially forms and indicating the various length scales is shown in Fig. 5. From Eq. (57), we note that $\mathcal{L}_{cap} \ll \tilde{\mathcal{L}}$ since $\delta \gg 1$.

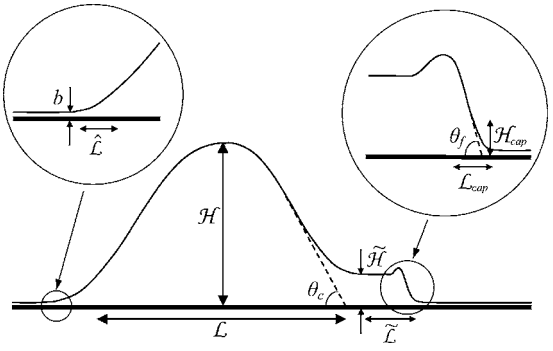

FIG. 5. Schematic illustration of the various relevant length scales describing the problem: $\mathcal{H}$ and $\mathcal{L}$ are the height and length scales of the original drop before activation of the electric field, $\tilde{\mathcal{H}}$ and $\tilde{\mathcal{L}}$ are the height and length scales in the electrowetting film over which the Maxwell stress decays, $\mathcal{H}_{cap}$ and $\mathcal{L}_{cap}$ are the electrocapillary height and length scales at the capillary ridge, and, b and $\hat{\mathcal{L}}$ are the Bretherton length scales describing the matching region between the drop and the precursor film. We note that $\mathcal{L} \gg \tilde{\mathcal{L}} \gg \mathcal{L}_{cap} \gg \hat{\mathcal{L}}$.

III. CONSTANT VOLUME SELF-SIMILAR SPREADING

It is possible to obtain a self-similar solution for the front-running electrowetting film by noting that θ_f and χ are constant. In this region, Maxwell stresses dominate and hence the axial capillary term in Eq. (49) can be neglected. In addition, if we consider the localized region near the tip such that $x_f - x \sim 0$ in Eq. (49), and since the contact angle θ_f has been shown to be locally constant, the Maxwell pressure gradient $p_x \sim -2\delta\chi$ is constant, resembling a constant body force similar to gravity. Equation (53) then reduces to a nonlinear hyperbolic equation given by

$$h_t = -2\delta\chi(h^3)_x/3. \tag{58}$$

If we adopt the transformation $h \sim x^\alpha t^\beta$, substitution into Eq. (58) above gives $\alpha = -\beta = 1/2$ and $1/\sqrt{2\delta\chi}$ for the coefficient of proportionality. It then follows that

$$h = \left(\frac{x}{2\delta\chi t}\right)^{1/2}. \tag{59}$$

Although it will be shown in Sec. V B that some liquid drainage occurs from the bulk macroscopic drop into the electrowetting film finger as it advances, this partial liquid drainage is small and will be shown to have negligible effect on the dynamics by which the film advances. As the Maxwell stress is localized to a region of length $\tilde{\mathcal{L}}$ at the tip near the contact line region, it is expected that no additional mass is extracted from the drop due to the Maxwell stress after the initial volume V_0 has been pulled out. We will therefore assume a constant volume of V_0 for the electrowetting film here but will correct for the small partial liquid drainage later in Sec. V B. Volume conservation then stipulates

$$V_0 = \int_0^{x_f} h\, dx, \tag{60}$$

where V_0 is the dimensionless version of the initial mass extracted, given by Eq. (42); we have scaled V_0 by $\tilde{\mathcal{H}}\tilde{\mathcal{L}}$ so that V_0 is an order 1 quantity. The film volume is shown to be a relatively constant value in the preliminary simulations with an average of approximately $V_0 = 0.763$, as depicted in

Fig. 4(b), with the exception of some small fraction originating from the drop. Although V_0 therefore has a slight dependence on the initial drop volume V_d, this dependence can be assumed negligible.

It is then possible to estimate the front shock position x_f:

$$x_f = \left(\frac{3V_0}{2}\right)^{2/3} (2\delta\chi t)^{1/3}. \tag{61}$$

Substituting Eq. (61) into Eq. (59) gives the self-similar behavior for the film height:

$$h_f = \left(\frac{3V_0}{2}\right)^{1/3} \frac{1}{(2\delta\chi t)^{1/3}}. \tag{62}$$

The $t^{1/3}$ behavior of the advancing front is analogous to that for planar gravity spreading obtained by Huppert [17] who solved Eq. (59) using the method of characteristics.

Reexpressing Eq. (61) in terms of dimensional quantities from the scalings adopted in Eq. (15), δ being defined by Eq. (26), we obtain

$$x_f = 0.4\left(\frac{\epsilon_0\epsilon_l V^2 R_e t}{\mu_l}\right)^{1/3}, \tag{63}$$

indicating that the position of the advancing front for the electrowetting film is independent of the dimensions and dynamics of the bulk macroscopic drop from which the film originates. x_f in Eq. (63) can also be expressed in terms of the electrocapillary time scale $\mathcal{T}_{cap} = \mu_l \mathcal{L}_{cap}/\gamma_l = \pi^2 \mu_l R_e / 8\epsilon_0\epsilon_l V^2$ using Eq. (56):

$$x_f = 0.43 R_e \left(\frac{t}{\mathcal{T}_{cap}}\right)^{1/3}. \tag{64}$$

The independence of the electrowetting finger dynamics of the drop dimension, capillarity, and wettability is a rather surprising result. The universal θ_f and the decay length of R_e where Maxwell pressure exists at the front have endowed this dynamics with insensitivity to the drop length scales.

Figure 6 shows a comparison of the advancing electrowetting film front position between the model prediction given in Eq. (64) with the planar electrowetting experiments of Ahmed *et al.* [16] using deionized water. Our $t^{1/3}$ predicted scaling compares reasonably well with the experimental data given the assumed planar film geometry and the absence of empirical fitting parameters. The slight disparity could possibly be due to lateral flow within the film which pushes liquid to the side contact lines thus further flattening the electrowetting film profile, which was observed to be more prevalent at low ac frequencies [15]; our one-dimensional model, nevertheless, cannot capture these effects. We will now proceed to validate this self-similar scaling with numerical results obtained from the lubrication model formulated that includes the macroscopic drop dynamics.

IV. NUMERICAL RESULTS

To include the dynamics of the macroscopic drop in our simulation of the full problem, we now scale the governing equations described by Eqs. (3)–(14) by the macroscopic drop dimensions, i.e.,

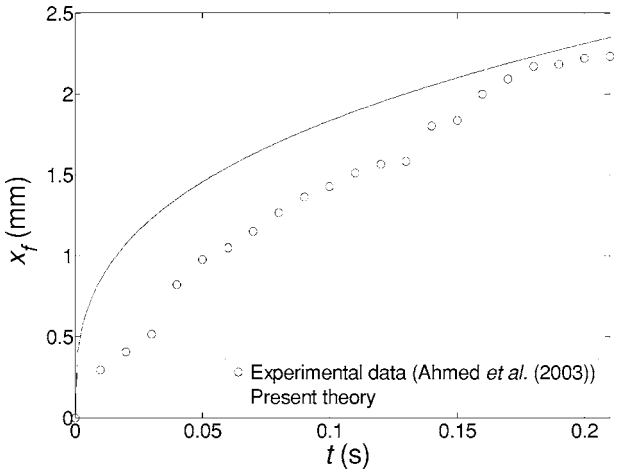

FIG. 6. Comparison of the theoretical prediction with the experimental data of Ahmed *et al.* [16] for the transient advancing position of the electrowetting film front x_f, indicating reasonable agreement between the present theory in Eq. (63) and experimental data without empirical fitting. The parameters used are $\mu_l = 1$ cP, $\epsilon_l = 78$, $\epsilon_g = 1$, $V = 200$ V, and $R_e = 40$ μm, corresponding to the experimental parameters used in [16]. We note that the spreading dynamics of the electrowetting film is independent of the drop volume $\mathcal{V}$.

$$x \to \mathcal{L}x, \quad y \to \mathcal{L}y, \quad \text{and} \quad (z,h) \to \mathcal{H}(z,h), \tag{65}$$

where $\mathcal{L}$ is the initial lateral and transverse extent of the drop in the x and y directions, and $\mathcal{H}$ is the initial height of the drop, before the electric field is activated. The drop is considered to be sufficiently slender such that $\varepsilon \equiv \mathcal{H}/\mathcal{L} \sim \tan\theta_c \ll 1$, where θ_c is the static contact angle, in order for the lubrication limit to hold. Moreover, the electrowetting film finger that is extracted is assumed to be narrow compared to the lateral dimension of the drop such that the radial geometry of the drop can be neglected. This one-dimensional planar model requires us to relate the true drop volume $\mathcal{V}$ to the volume per unit width V_d; we assume that the drop initially forms a spherical segment with volume $\mathcal{V} \sim \pi\mathcal{H}[\mathcal{H}^2 + (3\mathcal{L}^2/4)]$ and volume per unit width $V_d \sim \mathcal{H}\mathcal{L} \sim \mathcal{L}^2 \tan\theta_c$ such that

$$V_d \sim \left(\frac{6\mathcal{V}}{\pi \tan\theta_c \left(\frac{3}{4} + \tan^2\theta_c\right)}\right)^{2/3}. \tag{66}$$

In addition, we also scale u by $\mathcal{U} \equiv \tan^3\theta_c \gamma_l/\mu_l$, p by $\tan\theta_c \gamma_l/\mathcal{L}$, and t by $\mathcal{L}/\mathcal{U}$. These scalings together with the asymptotic expansions in Eq. (27) in the limit $\varepsilon \to 0$ render the same dimensionless leading order governing equations in Eqs. (49) and (53), but with δ and χ redefined as

$$\delta \equiv \frac{8\epsilon_0\epsilon_l V^2 \mathcal{L}}{\tan\theta_c \pi^2 \gamma_l R_e^2} = \frac{8\epsilon_0\epsilon_l - V^2}{\pi^2 \gamma_l R_e^2 (\tan\theta_c)^{3/2}} \left(\frac{3\mathcal{V}}{2\pi}\right)^{1/3} \tag{67}$$

and

$$\chi \equiv \frac{16 \tan^2 \theta_f \mathcal{L}^2}{R_e^2}, \tag{68}$$

respectively.

Equation (53) with Eq. (49) is solved subject to the no flux boundary conditions $h_x=0$ at $x=0$ and $x\to\infty$ and $h_{xxx}=0$ at $x=0$. To remove the contact line stress singularity, we assume the existence of a molecular front-running precursor film. This microscopic molecular precursor film is to be distinguished from the macroscopic electrowetting film finger that is formed due to the effects of the electric field. Justification of such precursor films for wetting drops is given in Appendix A. The remaining boundary condition is therefore dictated by the molecular precursor film thickness b, i.e., $h\to b$ as $x\to\infty$. The results in Appendix A show that the bulk wetting dynamics are insensitive to the precursor film thickness b. The precursor film, however, allows and facilitates the numerical resolution of the wetting dynamics.

The initial condition is specified by

$$h(x,0) = \xi_1\left[1 - \tanh\left(\frac{x-\xi_2}{\xi_3}\right)\right] + b, \tag{69}$$

where ξ_1, ξ_2, and ξ_3 are constants. In our numerical simulations, we take $\xi_2=1$ and $\xi_3=0.25$; other choices of these parameters that govern the slope of the profile only produced quantitatively different results. ξ_1 is varied to account for different drop volumes V_d; from numerical integration, we obtain $\xi_1 \sim V_d/2$. We adopt the method of lines [25] as our numerical scheme: Fourth-order centered differences are used to approximate the spatial derivatives, and Gear's method is used for the time integration [26]. Typically, 1000 grid points on a uniform grid for the spatial domain were used; convergence was achieved upon mesh refinement. The equations were also integrated using EPDCOL [27], which is based on finite element collocation for space and the method of lines in time; a uniform grid of 2000 grid points was typically used in the computations and perfect agreement was achieved between the results obtained from the two numerical procedures.

Typical spatiotemporal profiles for the spreading liquid drop under the action of the Maxwell stress are shown by the solid lines in Fig. 7(a). Since the normal Maxwell stress is localized in the tip region near the apparent contact line, a front-running electrowetting film is pulled out from the bulk of the drop and propagates faster than the drop itself. The advancing electrowetting film front is observed to form a capillary ridge, the height of which decreases in time as with the thickness of the electrowetting film behind it. However, the contact angle θ_f that the ridge makes with the solid substrate is time independent, consistent with our theory presented earlier. The height of the ridge is also observed to decrease with time as the total mass remains constant.

During a very short transient before the formation of the electrowetting film, the bulk drop spreads and decreases in height. This initial drop wetting dynamics is due to pure capillary spreading driven by the usual molecular wetting [28], prior to the formation and development of the electrowetting film. Once the electrowetting film is formed, the decrease in the height of the bulk drop is predominantly due to partial drainage of the liquid into the advancing electrowetting film. These mechanisms will be further elucidated in the next section when a matched asymptotic analysis between the bulk liquid drop and the electrowetting film is carried out. In contrast, there is no electrowetting film formation in the case when the Maxwell stress is absent, as shown by the profiles for pure capillary spreading indicated by the dashed lines in Fig. 7(a).

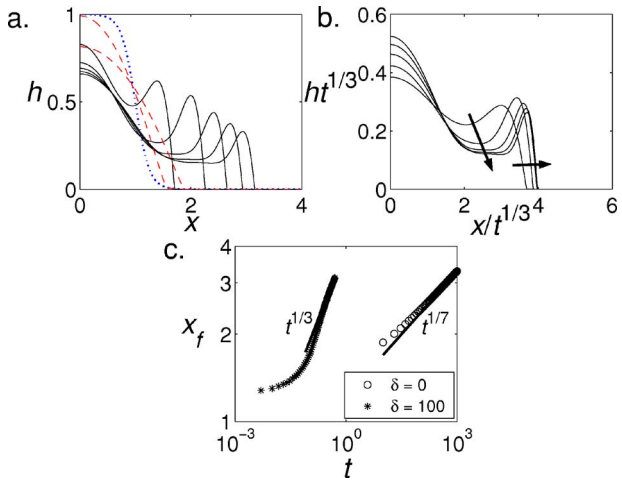

FIG. 7. (Color online) Numerical results of the wetting of a liquid drop on a solid horizontal substrate with $\delta=100$, $\chi=0.75$, $b=10^{-5}$, and $\xi_1=0.5$. (a) Typical profiles of the wetting drop and finger formation for five equal time steps up to $t=0.5$. (b) Replot of the data in (a) using a similarity transformation indicating the self-similar behavior of the advancing finger. (c) Position of the advancing front x_f as a function of t for Maxwell-dominated and pure capillary spreading. In (a) the dotted lines represent the initial drop profile and the dashed lines represent the case for pure capillary spreading where $\delta=0$ at times $t=1$ and 10; the arrows indicate the direction with increasing time. We note that the ridge height decreases in time but its intercept angle with the solid substrate θ_f is time independent.

The formation and propagation of the front-running electrowetting film takes place rapidly. In the case shown in Fig. 7(a), the film front advances by approximately 1.5 dimensionless units after $t=0.5$. In comparison, the dashed lines in Fig. 7(a) for the case $\delta=0$ where there is no Maxwell stress and the spreading of the bulk drop takes place by capillary pressure alone indicate that the apparent three-phase contact line only advances by approximately 0.25 dimensionless units after $t=10$. In Fig. 7(b), the evolution profiles for the spreading drop in Fig. 7(a) are replotted in the transformed coordinates given by Eqs. (61) and (62) showing the collapse of the front and film height profiles at long times. The progression of the advancing front x_f with time is captured in Fig. 7(c). It can be seen that the front spreads as $t^{1/3}$ for Maxwell-dominated spreading, consistent with the self-similar scaling laws derived in Sec. III, and as $t^{1/7}$ for pure capillary spreading driven by molecular wetting. The $t^{1/7}$ scaling is analogous to the classical $t^{1/10}$ scaling for pure capillary molecular driven spreading of axisymmetric drops first observed by Ausserré *et al.* [29] and can be obtained simply from the solution of the long-wave Laplace-Young

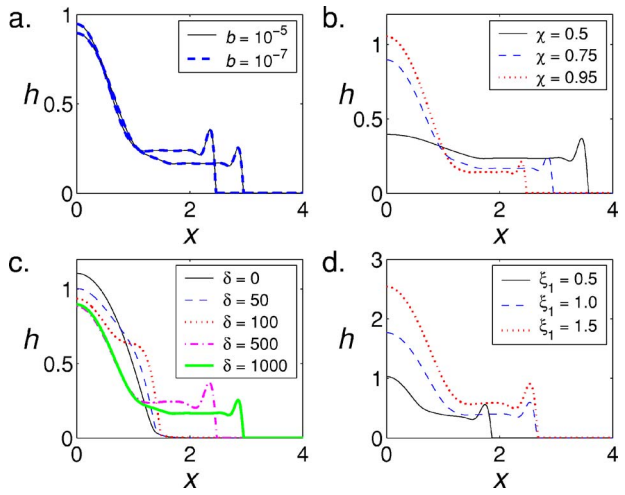

FIG. 8. (Color online) Parametric variations in the drop profiles for (a) the molecular precursor film thickness b at times $t=0.025$ and 0.05, (b) the Maxwell stress decay factor χ at $t=0.05$, (c) the Maxwell to capillary stress ratio δ at $t=0.05$, and (d) the initial volume of the drop defined by the parameter ξ_1 at $t=0.01$. Unless otherwise stated, the base parameters are $\delta=1000$, $\chi=0.75$, $\xi_1=0.5$, and $b=10^{-5}$.

equation $h^3h_{xxx}=0$, as will be shown in Sec. V. The appearance of this $t^{1/7}$ scaling in the initial spreading dynamics of the bulk drop, as proposed in our subsequent asymptotic matching in Sec. V, will thus suggest that it is pure capillary spreading driven by molecular wetting that dominates the bulk drop dynamics initially.

A sensitivity analysis of the numerical results on the various parameters is shown in Fig. 8. We confirm that the results in Fig. 8(a) show a weak dependence on the molecular precursor film thickness b, given that it is sufficiently thin. It will be shown in the following section that the $(-x)\log(-x)$ asymptotic precursor film behavior, x being the inner coordinate from an arbitrary cusp tip position in the precursor film, suggests a very weak dependence of the molecular precursor film thickness on the spreading dynamics of the macroscopic drop. We also explore the sensitivity of the spreading results to the linear Maxwell stress decay factor χ. Figure 8(b) indicates that the larger the fraction of the interface from the tip over which the Maxwell stress decays, the more rapid the spreading dynamics. The front is seen to propagate faster, giving rise to more slender films and a dilapidated drop. The contact angle at the advancing electrowetting film front can also be seen to be relatively independent of χ, consistent with our earlier findings in the preliminary simulations.

The effect of increasing δ is shown in Fig. 8(c). As δ increases, the Maxwell stress becomes increasingly dominant over capillary stresses therefore giving rise to faster spreading dynamics. We observe the critical Maxwell to capillary stress ratio $\delta_c \sim 10$ for the formation of the electrowetting film ahead of the drop. Above this critical value, the qualitative behavior of the spreading drop and the formation of the electrowetting film is similar; only the dynamics of these phenomena are affected by the value of δ. In the next section, it will be shown that the spreading dynamics can be collapsed by normalizing the time with δ suggesting that the Maxwell stress plays a role in stretching the electrowetting film in a self-similar manner. Figure 8(d) shows the dependence of the simulation results on the volume per unit width of the liquid drop V_d. We shall show in the following section that a generalized spreading condition can be derived by normalizing the drop height h by some power of V_d.

V. MATCHED ASYMPTOTIC ANALYSIS

In this section, we perform a matched asymptotic analysis to quantitatively model the electrocapillary spreading phenomena observed in the numerical simulations above. From our simulations, we note that there are two dynamics for the decreasing height of the bulk drop. Initially, the rate of decrease is rapid due to capillary spreading prior to the formation and development of the electrowetting film. Subsequently, the bulk drop dynamics slows down once the film is pulled out from the bulk. The decrease in the height of the bulk drop is then attributed to some drainage into the electrowetting film. We shall therefore perform a matched asymptotic analysis for the capillary spreading in Sec. V A, and, subsequently, a volumetric flow balance in Sec. V B.

A. Initial capillary spreading

For the initial molecular wetting driven spreading dominated by capillary action prior to the formation of the electrowetting film, the analysis is similar to the molecular precursor film model of Kalliadasis and Chang [28]. However, as discussed in Appendix A, having allowed for the existence of a precursor film, it is not necessary to include intermolecular effects. Neglecting the Maxwell stress, the matching region is governed by viscous and capillary forces alone and hence Eq. (53) can be written as

$$h_t = -(h^3h_{xxx})_x/3. \tag{70}$$

We now consider a locally quasisteady approximation in the bulk region with a constant dimensionless speed Ca, with respect to a coordinate frame moving slowly with the contact line by adopting the following transformation:

$$x^* = x - \mathrm{Ca}t. \tag{71}$$

Ca is the capillary number, defined as $\mathrm{Ca} \equiv \mu_l \mathcal{U}/\gamma_l$, which indicates the ratio of viscous to capillary stresses. The asterisk notation is dropped henceforth. In the locally quasisteady limit where the length scale of the precursor film region $\hat{\mathcal{L}}$ is much smaller than that of the macroscopic region $\mathcal{L}$, i.e., $\hat{\mathcal{L}}/\mathcal{L} \ll 1$, we then obtain the Bretherton equation [24]

$$3\mathrm{Ca}h_x = (h^3h_{xxx})_x. \tag{72}$$

Asymptotic matching between the inner molecular precursor film region and the outer bulk region and redimensionalizing subsequently yields

$$h \sim -x\mathrm{Ca}^{1/3}(9 \log \eta)^{1/3}, \tag{73}$$

from which a dynamic contact angle condition for the macroscopic drop θ_d can be derived [28]:

$$\tan\theta_d \sim -h_x \sim (-9\log\eta)^{1/3}\mathrm{Ca}^{1/3}, \tag{74}$$

the full derivation of which is given in Appendix B. In the above, $\eta=\hat{\mathcal{L}}/\mathcal{L}\sim b$ is a small parameter, b being the precursor film thickness. The $(-x)\log(-x)$ asymptotic behavior in Eq. (73) indicates a very weak dependence of the shape of the molecular precursor film on the spreading dynamics of the drop [28,30], which we observe to be true in our numerical simulations as shown in Fig. 8(a).

The outer solution describing the macroscopic dynamics of the bulk drop is given by the long-wave Laplace-Young equation $h^3h_{xxx}=0$ with boundary conditions $h_x=0$ at $x=0$ and $h=0$ at $x=x_d$, where x_d is the radius of the macroscopic drop. Imposing volume conservation on the drop, it is then possible to show (see Appendix B) that the solution of the long-wave Laplace-Young equation becomes

$$\tilde{x}_d = 1.458(\delta\chi V_0^2|\log\eta|)^{-1/7}\tilde{t}^{1/7}, \tag{75}$$

where

$$\tilde{x} = \frac{x}{V_d^{1/2}} \tag{76}$$

and

$$\tilde{t} = 2\delta\chi\left(\frac{3V_0}{2}\right)^2 t, \tag{77}$$

in which V_d is the drop volume. Equation (75), which governs the dynamics of pure capillary spreading driven by molecular wetting, therefore gives rise to the $t^{1/7}$ scaling obtained in Fig. 7(d) in the absence of any Maxwell stresses and hence electrowetting fingers.

We show in Appendix B that substitution of Eq. (75) into the quasisteady speed $3\mathrm{Ca}=\tilde{x}_{d_{\tilde{t}}}$ yields an expression for the drop height at $\tilde{x}=0$:

$$h(\tilde{x}=0) \sim (2\delta\chi)^{1/7}V_d^{1/2}\left(\frac{3V_0}{2}\right)^{2/7}\tilde{t}^{-1/7}. \tag{78}$$

The relevant scaling for the height of the bulk drop can now be determined:

$$\tilde{h} = \frac{h}{1.24(\delta\chi)^{1/7}V_d^{1/2}V_0^{2/7}}. \tag{79}$$

Equations (77) and (79) provide a set of scalings by which the data obtained in the numerical simulations can be collapsed. It then remains to predict the decrease in the macroscopic drop height by accounting for liquid drainage from the bulk into the electrowetting film.

B. Partial liquid drainage into the electrowetting film

Tracking the mass in the numerical results, we observe that the volume of the electrowetting film is not entirely conserved despite conservation of the overall volume. The growth rate of the finger volume is however constant. This therefore requires some small constant fraction ν of the initial electrowetting film volume V_0, taken to be constant [see Eq. (60)], to originate from bulk drainage into the film from the macroscopic liquid drop. For simplicity, we assume that the bulk of the liquid drop forms a hemisphere such that a volumetric flow balance reads

$$\frac{\pi}{4}\frac{d}{d\tilde{t}}(\tilde{h}^2) = -\nu\mathrm{Ca}h_f. \tag{80}$$

Normalizing the self-similar transforms in Eqs. (61) and (62) with Eq. (77), and utilizing these to integrate Eq. (80), we then arrive at

$$x_f = (4.5V_0^2\delta\chi t)^{1/3}, \tag{81}$$

which is simply the dimensionless version of Eq. (64), and

$$\tilde{h} = 0.804\nu^{1/2}V_0^{13/42}|\log\eta|^{-1/14}(\delta\chi t)^{-2/21}, \tag{82}$$

which is a dynamic condition for the decrease in the macroscopic drop height. In the above, ν is determined empirically from the numerical simulations and has a constant value of approximately 0.2; we therefore take ν to be a unit order universal coefficient. It will be shown that the numerical data can be collapsed using the set of scalings defined by Eqs. (79), (81), and (82).

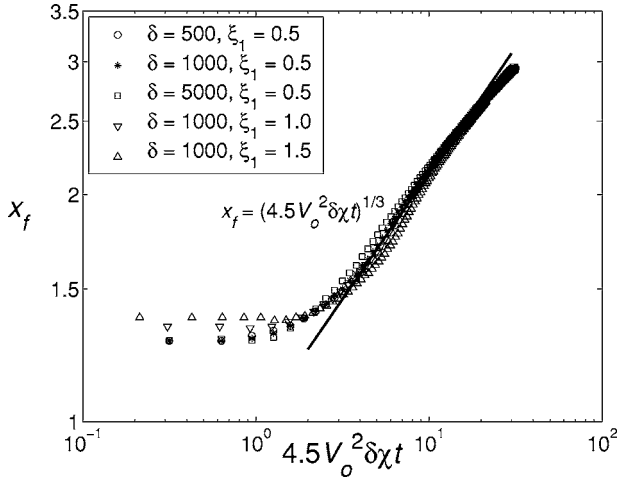

FIG. 9. Advancing front position of the electrowetting film x_f as a function of the normalized time $\tilde{t}$ for variations in δ and ξ_1, the latter adjusting for the drop volume V_d. The solid line represents $x_f=\tilde{t}^{1/3}=(4.5V_0^2\delta\chi t)^{1/3}$ indicating the collapse of the data with the normalized self-similar scaling in Eq. (81).

The advancing front position x_f and the normalized macroscopic drop height $\tilde{h}$ are plotted as functions of the normalized time $\tilde{t}=4.5V_0^2\delta\chi t$ in Figs. 9 and 10. The plots show the collapse of the numerical results for the variations in the parameters δ and V_d [parametrized by ξ_1 in Eq. (69)] with the scalings given by Eqs. (79), (81), and (82) from the analysis above. We have also plotted the $t^{1/7}$ behavior derived in Eq. (78) in Fig. 10 showing that this capillary-dominated scaling only applies in the initial transient spreading dynamics of the macroscopic drop. The self-similar scaling in Eq. (81) describes the behavior of the Maxwell-dominated advancing front in Fig. 9 well for large values of δ. For $\delta\ll 10^2$, some deviation from the self-similarity behavior depicted in Fig. 9 occurs due to the increasing domi-

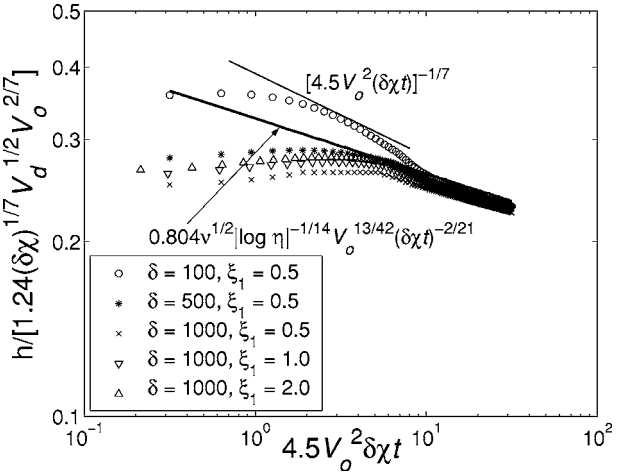

FIG. 10. Macroscopic drop height $\tilde{h}$ as a function of time $\tilde{t} = 4.5V_0^2\delta\chi t$ indicating the collapse of the normalized data obtained from the numerical simulations for parametric variations in δ and ξ_1, the latter responsible for adjusting the drop volume V_d, onto the dynamic spreading condition given by Eq. (82). The value of $\eta \sim b$, where b is the precursor film thickness is taken to be 10^{-7}, although its value is unimportant, as seen in Fig. 8(a).

nance of capillary stresses. On the contrary, when $\delta \gg 10^3$, the macroscopic drop height deviates from the normalization used in Fig. 10. In these large δ cases, the Maxwell stress overwhelms the capillary stresses and hence the assumption that capillary stresses dominate in the initial stages of the spreading breaks down. In any case, the collapse of the numerical data justify, over a moderate range of δ, the proposed mechanism based on initial capillary-dominated spreading followed by drainage of the bulk into the electrowetting film, and indicate that it is possible to quantitatively model the dynamic conditions of the advancing film and the spreading drop. It is also possible to obtain the transient for the formation of the front-running electrowetting film. From Fig. 10, we estimate the time for the electrowetting film to form to be $\sim 1/\delta\chi \sim 10^{-4}-10^{-3}$, corresponding to approximately $10^{-3}-10^{-2}$ s, which is negligible.

VI. CONCLUDING REMARKS

The spreading dynamics of a high permittivity polar dielectric liquid drop under the influence of electrocapillarity is studied both numerically and analytically. A pair of line electrodes is placed parallel to the direction of the flow similar to that used in the experiments of [15]. The liquid phase electric field is thus predominantly tangential to the contact line but without a longitudinal tangential field. Since the meniscus tip resembles a wedge whose contact angle is time invariant, the electric field decreases with increasing interfacial height, therefore producing a linearly decaying tangential interfacial field away from the tip defined by the apparent three-phase contact line with a decay length of roughly the electrode separation R_e. The longitudinal gradient of the resulting normal interfacial Maxwell pressure therefore drives a strong electrowetting flow. This Maxwell-stress-dominated spreading is reminiscent of gravity spreading and pulls out a thread of liquid film ahead of the bulk drop after a negligible transient time of approximately $10^{-3}-10^{-2}$ s. The film is dominated by a capillary ridge; the height of this capillary ridge decreases with time but the intercept angle it subtends with the solid substrate is independent of time. The liquid volume per unit width within the electrowetting film also remains constant at R_e^2. The front of this electrowetting film, in fact, advances as $t^{1/3}$ consistent with the self-similar gravity-driven fronts of Huppert [17]. Like gravity spreading, it is independent of capillarity and wettability. On the other hand, the finger dynamics is independent of the drop volume unlike in gravity spreading. Our prediction for the position of the electrowetting film front is also close to the finger advancing dynamics observed in the electrowetting experiments of Ahmed *et al.* [16]. The numerical results, obtained by solving for the mass and momentum conservation of the fluid flow in the lubrication limit, together with the normal stress jump containing the Maxwell stress contribution and the appropriate initial and boundary conditions, demonstrate this similarity behavior. This spreading dynamics is much faster than the classical wetting scaling of $t^{1/7}$ due to molecular wetting.

By employing a matched asymptotic analysis between the molecular precursor film and the macroscopic bulk of the liquid drop, we were able to determine the relevant scalings for the initial capillary-dominated molecular driven spreading of the drop prior to the formation of the electrowetting film, the bulk of the drop spreading as $t^{1/7}$. The matching also stipulated a contact angle condition for the slope that scales as $\mathrm{Ca}^{1/3}$, in agreement with Tanner's law. The numerical simulations however indicated that the $t^{1/7}$ spreading slowed down once the film is pulled out ahead of the drop after a transient time of $10^{-3}-10^{-2}$ s and revealed a small constant fraction $\nu \sim 0.2$ of the electrowetting film finger originating due to drainage from the bulk of the macroscopic drop. By normalizing the data using the scalings obtained from the matched asymptotics, the final condition for the drop height which decreases as $t^{-2/21}$ was obtained from a volumetric balance, from which we obtain good agreement with the collapsed numerical data from the normalization. The consistency between the numerical and analytical results lends credibility to our proposed mechanism: The initial spreading of the drop prior to formation of the electrowetting film is dominated by the capillary stresses; the normal Maxwell stress plays a role in pulling out the electrowetting film ahead of the drop. Once the film is developed, however, the Maxwell stress dominates at the advancing front of the electrowetting film and the bulk of the drop spreads due to partial drainage into the film. This spreading is accelerated by the formation of the electrowetting film which prewets the substrate in a similar manner to the molecular precursor film. In contrast to the molecular precursor film, however, this electrowetting film is macroscopic whose front advances much faster due to Maxwell-dominated spreading than for the case of liquid spreading due to capillary pressure, thus suggesting that the electrode configuration proposed produces a strong electrowetting effect. We observe the position of the advancing film front to scale quadratically with respect to the applied voltage, consistent with the experimental data reported in the literature.

ACKNOWLEDGMENTS

This work was partially supported by the U.S. Army CECOM RDEC through Agreement DAAB07-03-3-K414. We are grateful to T. B. Jones for helpful discussions on the electrostatic formulation.

APPENDIX A: MOLECULAR PRECURSOR FILM MODEL AND SLIP CONDITIONS

Wetting is driven by molecular forces at the contact line. However, there is considerable evidence that for highly wetting fluids with small dynamic contact angles θ_d, such molecular dynamics can be captured by macroscopic slip models using continuum descriptions [28,31–33], in which the slip coefficients and the exact form of the slip condition have been thoroughly investigated. An alternative model for perfectly wetting fluids is to precoat the surface with a film during the simulation of wetting dynamics [18], as is done in the present approach. Thin molecular precursor films, where liquid from the bulk of the drop drains into due to the negative disjoining and capillary pressures, have indeed been observed experimentally using ellipsometry for wetting fluids [29], as well as in molecular dynamic simulations [34]. Although the precursor film is much thinner than the macroscopic precursor film used in most simulations, Kalliadasis and Chang [28] have shown that the thickness of this precursor film does not significantly affect the wetting dynamics. The key parameter is the precursor film thickness. We show in the arguments to follow that the precursor film model produces the same bulk asymptotic dynamics as the slip models and that the precursor film can be related to the slip coefficient of a continuum slip model. More importantly, the slip coefficient is insensitive to the precursor film thickness and hence justifies the use of a macroscopic precursor film in our simulations. Consequently, even if a precursor film does not exist in reality, the precursor film model can be adequately used to simulate wetting in a numerical study.

The arguments here follow from Kalliadasis and Chang [28] where the disjoining pressure arising from long-range intermolecular interactions were introduced into the Bretherton equation [Eq. (72)] for the film near the contact line:

$$3\mathrm{Ca}h_x = \left[h^3 h_{xxx} - h^3 \left(\frac{\alpha}{6\pi\gamma_l h^3} - \frac{\beta h_x^4}{\gamma_l h^3} \right)_x \right]_x, \tag{A1}$$

where α is the Hamaker constant and β is a parameter that accounts for nonparallel effects [35]. Following Joanny [36], we omit the β term; scaling h and x with the characteristic height and length scales of the precursor film, $\hat{\mathcal{H}}_p$ and $\hat{\mathcal{L}}_p$, respectively, where $\hat{\mathcal{H}}_p \equiv \sqrt{-\alpha/6\pi\gamma_l}/(3\mathrm{Ca})^{1/3}$ and $\hat{\mathcal{L}}_p \equiv \sqrt{-\alpha/6\pi\gamma_l}/(3\mathrm{Ca})^{2/3}$, then yields

$$h^3 h_{xxx} = h + 3(h_x/h), \tag{A2}$$

where the second term on the right arises due to intermolecular forces.

In the asymptotic limit away from the inner contact line region toward the bulk region where $h \to \infty$ as $x \to -\infty$, the h_x/h term on the right side of Eq. (A2), which arises due to intermolecular forces, drops out and we obtain

$$h_{xxx} = 1/h^2, \tag{A3}$$

for which there are two asymptotic solutions [37]:

$$h_x(x \to -\infty) \sim -\sqrt{2(h-e)} + \frac{2}{3h} + \frac{2e}{45h^2} \tag{A4}$$

and

$$h(x \to -\infty) \sim 3^{1/3}(-x)[\log(-x) - c]^{1/3}, \tag{A5}$$

where c and e are constants of order 1. Given the quadratic behavior of h as $x \to -\infty$ due to the singularity of Eq. (A4) when $h_{xx} \to 0$ at large x, we admit the logarithmic asymptotic behavior in Eq. (A5) with $c = 1.026$ as our solution of Eq. (A3); a further discussion of this choice and when Eq. (A4) should be used can be found in Kalliadasis and Chang [28].

On the other hand, a dominant balance between the intermolecular and viscous terms on the right side of Eq. (A2) stipulates the asymptotic behavior of the inner contact line region as $x \to \infty$:

$$h_x = -h^2, \tag{A6}$$

which yields the following hyperbolic behavior [28]:

$$h(x \to \infty) \sim \frac{3}{x} + \frac{6}{5(x/3)^{1/7}} + c_1 \exp\left(\frac{(x/3)^3}{3} \right), \tag{A7}$$

where c_1 is a constant. The first term was derived by Voinov [38] and the exponential term was added by Hervet and de Gennes [39]; the second term on the right, nevertheless, dominates over this exponential term. Asymptotic matching between the outer and inner solutions, given by Eqs. (A5) and (A7), respectively, and redimensionalizing, then yields

$$h \sim -x\mathrm{Ca}^{1/3} \left(9 \log \sqrt{\frac{|\alpha|}{6\pi\gamma_l}} \right)^{1/3}. \tag{A8}$$

A comparison with the solution for the precursor film model in Eq. (73) then shows that the small parameter in the dynamic contact angle condition [Eq. (74)],

$$\eta = \frac{1}{\mathcal{L}} \sqrt{\frac{|\alpha|}{6\pi\gamma_l}}, \tag{A9}$$

is equivalent to the molecular precursor film thickness b. This therefore suggests that the disjoining pressure can be approximated by the precursor film thickness. In other words, the precursor film model is a reasonable approximation to account for intermolecular effects.

We now proceed to show that the use of slip models also give rise to similar asymptotic behavior away from the contact line. Here, we adopt the Navier slip boundary condition [33]

$$3u = \lambda(h) u_z \quad \text{at } x = 0, \tag{A10}$$

where u is the slip velocity and $\lambda = \lambda_i / h^i$ is the slip length that is dependent on the film thickness h. $i = 0, 1$ corresponds to different slip models which have been used historically [33]. The incorporation of Eq. (A10) then modifies the quasisteady lubrication approximation in Eq. (72) to

$$3\mathrm{Ca}h_x = \left[h^2 \left(h + \frac{\lambda_i}{h^i} \right) h_{xxx} \right]_x . \tag{A11}$$

Adopting the transformations $h \to \lambda_i^{1/(1+i)} h$ and $x \to \lambda_i^{1/(1+i)} x/(3\mathrm{Ca})^{1/3}$, Eq. (A11) becomes

$$h_{xxx} = \frac{1}{h(h+h^{-1})} . \tag{A12}$$

A further boundary condition at the contact line is required. We will restrict our analysis to the case of perfectly wetting liquids such that

$$h_x = 0 \quad \text{at } x = 0 \tag{A13}$$

can be imposed. Analysis of partially wetting fluids as well as other boundary conditions have been carried out by Kalliadasis [40]; these however were shown to result in the same conclusions we present below.

For $h \ll 1$, Eq. (A12) reduces to $h^{i-1} h_{xxx} \sim 1$, which has the following asymptotic solution as $x \to \infty$:

$$h(x \to \infty) \sim 3^{1/3}(-x)[\log(-x) + c_i]^{1/3}, \tag{A14}$$

where c_i is a constant obtained by satisfying the boundary condition in Eq. (A13). By matching Eq. (A14) to the asymptotic solution of the outer region away from the slip plane given by Eq. (A5), and redimensionalizing, we obtain

$$h \sim -x\mathrm{Ca}^{1/3} \left(9 \log \frac{(3\mathrm{Ca})^{1/3}}{\lambda_i^{1/(1+i)}} + 9c_i \right). \tag{A15}$$

As λ_i and Ca approach zero, $\lambda_i^{1/(1+i)}/(3\mathrm{Ca})^{1/3} \to 0$, and hence the contact angle condition to leading order becomes

$$\tan\theta_d \sim -h_x \sim (-9 \log \lambda_i^{1/(1+i)})^{1/3} \mathrm{Ca}^{1/3}. \tag{A16}$$

A comparison between Eqs. (74) and (A16) then suggests

$$\lambda_i \sim \eta^{1+i}, \tag{A17}$$

i.e., the slip coefficient is shown to be equivalent to molecular length scale. Kalliadasis [40] showed that the same result is obtained for a more generalized boundary condition involving a velocity dependent contact angle [41] as well as for partially wetting liquids.

The analysis above therefore suggests that the asymptotic behavior of the inner region where intermolecular forces are dominant is universal and not dependent on any particular mechanism utilized to remove the contact line stress singularity. The intermolecular forces are shown to be solely determined by the apparent dynamic contact angle and is independent of slip to leading order. The precursor film and slip models, while mathematically expedient for removing the singularity, do not contribute to the apparent dynamic contact angle. Because of the weak dependence of the coefficient $(-9 \log \eta)^{1/3}$ on the asymptotic behavior of the height of the bulk region, imposing one or the other does not contribute to any significant error.

In summary, these findings indicate that for perfectly or partially wetting fluids, the asymptotic behavior of the outer region is universally independent of the specific model used to remove the contact line discontinuity because viscous and capillary stress balance in the vicinity where the outer region approaches the solid substrate. The existence and location of the tip of the molecular precursor film is therefore unimportant as far as the dynamic contact angle is concerned to leading order.

APPENDIX B: DERIVATION OF ASYMPTOTIC EQUATIONS FOR CAPILLARY SPREADING AND ELECTROWETTING FILM FORMATION

In the locally quasisteady limit with respect to the moving coordinate frame described by the transformation in Eq. (71), the film height evolution equation in Eq. (70), in which a dominant balance between viscous and capillary forces occurs in the matching region between the molecular precursor film and the bulk drop, reduces to

$$h_t - \mathrm{Ca}h_x = -(h^3 h_{xxx})_x/3 . \tag{B1}$$

The first term on the left, of order $\mu_l \hat{\mathcal{H}}/\mathcal{T}$, represents the transient dynamics of the molecular precursor film during the spreading whereas the second term, of order $\mu_l \mathcal{U} \hat{\mathcal{H}}/\gamma_l \hat{\mathcal{L}}$, represents the viscous effects due to steady translation of the interface. $\hat{\mathcal{H}}$ and $\hat{\mathcal{L}}$ are the characteristic height and length scales in the contact angle matching region between the bulk of the drop and the molecular precursor film, respectively, and $\mathcal{T}$ represents the characteristic time scale for spreading. We note that the quasisteady approximation breaks down when the ratio of the first and second terms on the left hand side of Eq. (B1), which is equal to the ratio of the length scales of the macroscopic and precursor film regions $\mathcal{L}/\hat{\mathcal{L}}$, becomes comparable. Considering the locally quasisteady case where $\hat{\mathcal{L}}/\mathcal{L} \ll 1$, we therefore obtain the Bretherton equation in Eq. (72) from Eq. (B1).

Rescaling h by the molecular precursor film thickness b and x by $\hat{\mathcal{L}} = b/(3\mathrm{Ca})^{1/3}$, and noting that the asymptotic behavior away from the inner molecular precursor film region towards the outer bulk region blows up, i.e., $h \to \infty$ as $x \to -\infty$, we recover Eq. (A3) from Eq. (72), which has an asymptotic solution given by Eq. (A5). Redimensionalizing, and utilizing a small parameter $\eta = \hat{\mathcal{L}}/\mathcal{L} \sim b$, where b is the precursor film thickness, yields

$$h \sim -x\mathrm{Ca}^{1/3}(9 \log \eta)^{1/3}, \tag{B2}$$

which yields a condition for the contact angle for the macroscopic drop θ_d [28]

$$\tan\theta_d \sim -h_x \sim (-9 \log \eta)^{1/3} \mathrm{Ca}^{1/3}. \tag{B3}$$

The outer solution describing the macroscopic dynamics of the bulk drop is given by the long-wave Laplace-Young equation $h^3 h_{xxx} = 0$ with boundary conditions $h_x = 0$ at $x = 0$ and $h = 0$ at $x = x_d$, where x_d is the radius of the macroscopic drop. A further boundary condition for volume conservation stipulates that

$$V_d = \int_0^{x_d} h \, dx, \tag{B4}$$

from which we obtain an expression describing the static circular drop:

$$h = \frac{3V_d}{2x_d^3}(x_d^2 - x^2). \tag{B5}$$

It then follows that

$$h_x(x = x_d) = -\frac{3V_d}{x_d^2}. \tag{B6}$$

Normalizing the self-similar transforms in Eqs. (61) and (62) with

$$\tilde{t} = 2\delta\chi\left(\frac{3V_0}{2}\right)^2 t, \tag{B7}$$

we arrive at

$$x_f = \tilde{t}^{1/3} \tag{B8}$$

and

$$h_f = \frac{3V_0}{2}\tilde{t}^{-1/3}. \tag{B9}$$

We utilize the quasisteady speed

$$3\mathrm{Ca} = \tilde{x}_{d_t}, \tag{B10}$$

where $\tilde{x}=x/V_d^{1/2}$, in the matching of the molecular precursor film and the macroscopic liquid drop in Eqs. (B3) and (B6) at $x=\tilde{x}_d$. This leads to

$$\frac{27}{\tilde{x}_d^6} = 4.5(-3\log\eta)\delta\chi V_0^2\frac{d\tilde{x}_d}{d\tilde{t}}, \tag{B11}$$

which can be integrated to give

$$\tilde{x}_d = 1.458(\delta\chi V_0^2|\log\eta|)^{-1/7}\tilde{t}^{1/7}. \tag{B12}$$

Substitution of Eq. (B12) into Eq. (B10) then gives an expression for the local quasisteady speed:

$$\mathrm{Ca} = 0.086|\log\eta|^{-1/7}\tilde{t}^{6/7}. \tag{B13}$$

The relevant scaling for the height of the bulk drop can also now be determined. From Eq. (B5) with $\tilde{x}=0$ and Eq. (B12),

$$h(\tilde{x}=0) \sim (2\delta\chi)^{1/7}V_d^{1/2}\left(\frac{3V_0}{2}\right)^{2/7}\tilde{t}^{-1/7}, \tag{B14}$$

so that

$$\tilde{h} = \frac{h}{(2\delta\chi)^{1/7}V_d^{1/2}(3V_0/2)^{2/7}}. \tag{B15}$$

Substitution of Eqs. (B9) and (B13) into the film volumetric flow balance in Eq. (80) and integrating then gives the dynamic condition for the decrease in the drop height:

$$\tilde{h} = 0.758\left(\frac{3\nu V_0}{2}\right)^{1/2}|\log\eta|^{-1/14}\tilde{t}^{-2/21}. \tag{B16}$$

More explicitly, Eqs. (B8), (B15), and (B16) can be written as

$$x_f = (4.5V_0^2\delta\chi t)^{1/3}, \tag{B17}$$

$$\tilde{h} = \frac{h}{1.24(\delta\chi)^{1/7}V_d^{1/2}V_0^{2/7}}, \tag{B18}$$

and

$$\tilde{h} = 0.804\nu^{1/2}V_0^{13/42}|\log\eta|^{-1/14}(\delta\chi t)^{-2/21}, \tag{B19}$$

respectively.

Reconverting Eqs. (B18) and (B19) to dimensional form, and using Eq. (66) to relate the volume per unit width V_d in our one-dimensional planar model to the true drop volume $\mathcal{V}$, we obtain

$$\tilde{h} = 0.622h\left(\frac{\gamma_l\left(\frac{3}{4}+\tan^2\theta_c\right)^2}{\epsilon_0\epsilon_l V^2\mathcal{V}^2\tan^2\theta_c}\right)^{1/7} \tag{B20}$$

and

$$\tilde{h} = 0.104R_e\left|\log\left(\frac{0.873\pi^{1/3}b\sqrt{\tan\theta_c}}{\mathcal{V}^{1/3}}\right)\right|^{-1/14} \times\left(\frac{\mu_l\left(\frac{3}{4}+\tan^2\theta_c\right)^{17/6}}{\epsilon_0\epsilon_l V^2\mathcal{V}^{17/6}(\tan\theta_c)^{29/12}t}\right)^{2/21}. \tag{B21}$$

[1] M. W. J. Prins, W. J. J. Welters, and J. W. Weekamp, Science **291**, 277 (2001).
[2] T. D. Blake, A. Clarke, and E. H. Stattersfield, Langmuir **16**, 2928 (2000).
[3] B. Berge and J. Peseux, Eur. Phys. J. E **3**, 159 (2000).
[4] C. Decamps and J. De Coninck, Langmuir **16**, 10150 (2000).
[5] B. Janocha, H. Bauser, C. Oehr, H. Brunner, and W. Göpel, Langmuir **16**, 3349 (2000).
[6] G. Lippmann, Ann. Chim. Phys. **5**, 494 (1875).
[7] M. J. de Ruijter, T. D. Blake, and J. De Coninck, Langmuir **15**, 7836 (1999).
[8] R. Digilov, Langmuir **16**, 6719 (2000).
[9] T. Chou, Phys. Rev. Lett. **87**, 106101 (2001).
[10] K. H. Kang, I. S. Kang, and C. M. Lee, Langmuir **19**, 9334 (2003).
[11] J. Buehrle, S. Herminghaus, and F. Mugele, Phys. Rev. Lett. **91**, 086101 (2003).
[12] M. Valet, M. Vallade, and B. Berge, Eur. Phys. J. B **11**, 583 (1999).
[13] K. H. Kang, Langmuir **18**, 10318 (2002).
[14] L. Y. Yeo and H.-C. Chang, Mod. Phys. Lett. B **19**, 549 (2005).
[15] T. B. Jones, M. Gunji, M. Washizu, and M. J. Feldman, J. Appl. Phys. **89**, 1441 (2001).
[16] R. Ahmed, D. Hsu, C. Bailey, and T. B. Jones, in Proceedings of the 1st International Conference on Microchannels and Min-

ichannels ICMM2003-1110, S. Kandlikar (ASME, Rochester, NY, 2003).
[17] E. Huppert, Nature (London) **300**, 427 (1982).
[18] S. M. Troian, E. Herbolzheimer, S. A. Safran, and J. F. Joanny, Europhys. Lett. **10**, 25 (1989).
[19] S. C. Landau and E. M. Lifshitz, *Electrodynamics of Continuous Media* (Pergamon, Oxford, 1960).
[20] J. R. Melcher, *Continuum Electromechanics* (MIT Press, Cambridge, MA, 1981).
[21] A. Indeikina, I. Veretennikov, and H.-C. Chang, J. Fluid Mech. **338**, 173 (1997).
[22] J. M. Davis, Phys. Fluids **17**, 038101 (2005).
[23] E. Kreyszig, *Advanced Engineering Mathematics* (Wiley, New York, 1999).
[24] F. P. Bretherton, J. Fluid Mech. **10**, 166 (1961).
[25] W. E. Schiesser, *The Numerical Method of Lines* (Academic, San Diego, 1991).
[26] O. K. Matar and S. M. Troian, Phys. Fluids **11**, 3232 (1999).
[27] P. Keast and P. H. Muir, ACM Trans. Math. Softw. **17**, 153 (1991).
[28] S. Kalliadasis and H.-C. Chang, Ind. Eng. Chem. Res. **35**, 2860 (1996).
[29] D. Ausserré, A. M. Picard, and L. Léger, Phys. Rev. Lett. **57**, 2671 (1986).
[30] S. Kalliadasis and H.-C. Chang, Phys. Fluids **6**, 12 (1994).
[31] L. M. Hocking, J. Fluid Mech. **77**, 209 (1977).
[32] P. G. de Gennes, Rev. Mod. Phys. **57**, 827 (1985).
[33] P. J. Haley and M. J. Miksis, J. Fluid Mech. **223**, 57 (1991).
[34] J. A. Nieminen, D. B. Abraham, M. Karttunen, and K. Kaski, Phys. Rev. Lett. **69**, 124 (1992).
[35] C. A. Miller and E. Ruckenstein, J. Colloid Interface Sci. **48**, 368 (1974).
[36] J. F. Joanny, J. Theor. Appl. Mech. **271**, 249 (1986).
[37] C. M. Bender and S. A. Orszag, *Advanced Mathematical Methods for Scientists and Engineers* (McGraw-Hill, New York, 1978).
[38] O. V. Voinov, J. Appl. Mech. Tech. Phys. **2**, 92 (1977).
[39] H. Hervet and P. G. de Gennes, C. R. Acad. Sci., Ser. II: Mec., Phys., Chim., Sci. Terre Univers **299**, 499 (1984).
[40] S. Kalliadasis, Ph.D. thesis, University of Notre Dame, 1994 (unpublished).
[41] L. M. Hocking, J. Fluid Mech. **239**, 671 (1992).